ADVANCES IN ATMOSPHERIC SCIENCES, VOL. 39, JANUARY 2022, 55–66

• Original Paper •

Ocean Response to a Climate Change Heat-Flux Perturbation in an Ocean Model and Its Corresponding Coupled Model

Jiangbo JIN[1,2], Xiao DONG[1], Juanxiong HE[1], Yi YU[2], Hailong LIU*[3,4], Minghua ZHANG[5], Qingcun ZENG[1], He ZHANG[1], Xin GAO[1], Guangqing ZHOU[1], and Yaqi WANG[3,4]

[1]*International Center for climate and Environment Sciences (ICCES), Institute of Atmospheric Physics, Chinese Academy of Sciences, Beijing* 100049, *China*

[2]*State Key Laboratory of Satellite Ocean Environment Dynamics, Second Institute of Oceanography, Ministry of Natural Resources, Hangzhou* 310012, *China*

[3]*State Key Laboratory of Numerical Modeling for Atmospheric Sciences and Geophysical Fluid Dynamics (LASG), Institute of Atmospheric Physics, Chinese Academy of Sciences, Beijing* 100049, *China*

[4]*College of Earth and Planetary Sciences, University of Chinese Academy of Sciences, Beijing* 100049, *China*

[5]*School of Marine and Atmospheric Sciences, Stony Brook University, Stony Brook, New York, NY* 11790, *USA*

(Received 4 May 2021; revised 11 August 2021; accepted 17 August 2021)

ABSTRACT

State-of-the-art coupled general circulation models (CGCMs) are used to predict ocean heat uptake (OHU) and sea-level change under global warming. However, the projections of different models vary, resulting in high uncertainty. Much of the inter-model spread is driven by responses to surface heat perturbations. This study mainly focuses on the response of the ocean to a surface heat flux perturbation F, as prescribed by the Flux-Anomaly-Forced Model Intercomparison Project (FAFMIP). The results of ocean model were compared with those of a CGCM with the same ocean component. On the global scale, the changes in global mean temperature, ocean heat content (OHC), and steric sea level (SSL) simulated in the OGCM are generally consistent with CGCM simulations. Differences in changes in ocean temperature, OHC, and SSL between the two models primarily occur in the Arctic and Atlantic Oceans (AA) and the Southern Ocean (SO) basins. In addition to the differences in surface heat flux anomalies between the two models, differences in heat exchange between basins also play an important role in the inconsistencies in ocean climate changes in the AA and SO basins. These discrepancies are largely due to both the larger initial value and the greater weakening change of the Atlantic meridional overturning circulation (AMOC) in CGCM. The greater weakening of the AMOC in the CGCM is associated with the atmosphere–ocean feedback and the lack of a restoring salinity boundary condition. Furthermore, differences in surface salinity boundary conditions between the two models contribute to discrepancies in SSL changes.

Key words: ocean heat uptake, Atlantic meridional overturning circulation, ocean general circulation model, coupled general circulation model

Citation: Jin, J. B., and Coauthors, 2022: Ocean response to a climate change heat-flux perturbation in an ocean model and its corresponding coupled model. *Adv. Atmos. Sci.*, **39**(1), 55–66, https://doi.org/10.1007/s00376-021-1167-y.

Article Highlights:

- The ocean response to prescribed heat-flux perturbation in an ocean model and its corresponding coupled model is investigated.
- The OHU, DSL simulated in the OGCM are generally consistent with CGCM simulations on the global scale.
- Differences in changes in ocean temperature, OHC, and SSL between the two models primarily occur in AA and SO basins.

1. Introduction

Ocean heat uptake (OHU), which refers to the change in ocean heat content (OHC), leads to the thermal expansion of seawater and thus contributes to sea level rise (Kuhlbrodt and Gregory, 2012; Church et al., 2013). However, gaps in observational data in the deep ocean and the Southern Ocean (SO) make it difficult to estimate OHU (Garuba and Klinger, 2016). Therefore, atmosphere–ocean coupled

* Corresponding author: Hailong LIU
Email: lhl@lasg.iap.ac.cn

models are widely used to investigate ocean climate changes (including changes in OHC, sea level, and ocean circulation) in response to increases in anthropogenic CO_2. Increases in atmospheric CO_2 result in perturbations in heat, freshwater, and momentum fluxes at the oceanic surface, which can further cause changes to OHC through both thermodynamic and dynamic processes (Rahmstorf and Ganapolski, 1999; Gregory et al., 2005, 2016; Bouttes and Gregory, 2014).

Recently, Huber and Zanna (2017) showed that perturbations in surface flux are major sources of spread among model estimates of OHU, especially surface heat flux perturbations. To reduce errors resulting from coupled models in the simulation and projection of OHU and sea-level rise in response to a doubled CO_2 concentration, the Coupled Model Intercomparison Project Phase 6 (CMIP6) launched the Flux-Anomaly-Forced Model Intercomparison Project (FAFMIP) to compare the responses of different models to the same surface flux perturbations (Gregory et al., 2016). Surface flux perturbations (including surface heat, freshwater, and momentum perturbations) in FAFMIP are derived from the ensemble mean differences between years 61 and 80 of the 13 CMIP5 atmosphere–ocean coupled models of a 1pctCO2 scenario experiments (corresponding to doubled CO_2 concentration) and from all years of piControl simulations and fixed seasonal cycles. FAFMIP experiments can be carried out with both Coupled General Circulation Models (CGCMs) and stand-alone Ocean General Circulation Models (OGCMs). However, few papers have focused on differences in results between OGCMs and CGCMs besides Todd et al. (2020).

Stand-alone OGCMs have been employed in the past to investigate ocean climate changes in response to increases in atmospheric CO_2. Xie and Vallis (2012) used a simplified OGCM to show the importance of the redistributive effect of heat due to the weakening of the Atlantic Meridional Overturning Circulation (AMOC) in determining the spatial pattern of OHU. Garuba and Klinger (2016) designed different methods to isolate and quantify the contribution of the redistributive component to the total amount of OHU in a stand-alone ocean model. They found that most of the heat uptake in the North Atlantic is due to the weakening of the AMOC. Garuba and Klinger (2018) used an ocean model to isolate the impacts of each surface flux perturbation (including the heat flux, wind stress, and freshwater) on the OHU. Their model assumes that the total ocean circulation response due to all surface flux perturbations can be regarded as the sum of changes caused by each surface perturbation. Marshall et al. (2014) employed an OGCM to show that changes in surface temperature due to global warming in a simplified ocean-only model are similar to the ensemble mean changes of 15 coupled climate models from CMIP5. All of the experiments above show similar results to those reported by FAFMIP (Gregory et al., 2016), but they used different methods to separate the effect of the ocean dynamics and different forcing fluxes at the surface. Therefore, it is also necessary to understand the similarities and differences in FAFMIP experiments between OGCM and CGCM simulations in the projections of ocean climate changes. Previous studies have shown that ocean climate changes in response to CO_2 forcing are primarily determined by the uptake of surface heat flux perturbations (Garuba and Klinger, 2018; Gregory et al., 2016; Jin et al., 2021). Furthermore, much of the inter-model spread is also driven by the response to surface heat perturbations (Todd et al., 2020). Therefore, in this study, we investigated the similarities and differences in the projections of ocean climate changes between coupled and uncoupled models by using the FAFMIP heat flux perturbation experimental protocol and dataset. To quantify the contribution of ocean circulation, the decomposition method of Gregory et al. (2016) was adopted.

The paper proceeds as follows. The methods and experimental design are described in section 2. The results are presented in section 3, followed by a summary and discussions in section 4.

2. Models, experiments, and methods

2.1. *Models*

The simulations in this paper were performed using a stand-alone OGCM and a CGCM with the same oceanic component. Here, the OGCM is the second revised version of the LASG/IAP (State Key Laboratory of Numerical Modeling for Atmospheric Sciences and Geophysical Fluid Dynamics/Institute of Atmospheric Physics) Climate System Ocean Model (LICOM2.0) (Liu et al., 2012; Dong et al., 2021a). The model domain is global with approximately 1° horizontal resolution, with a 0.5° meridional resolution between 10°S and 10°N. There are 30 levels in the vertical direction, with 10 m per layer in the upper 150 m. The second-order vertical turbulent mixing scheme is applied (Canuto et al., 2001, 2002). The scheme of Gent and McWilliams (1990), which uses a diffusion coefficient of 1000 $m^2\ s^{-1}$ for both the bolus and Redi parts, is used for the isopycnal mixing. Convection is parameterized by convective adjustment (Pacanowski, 1995). The sea surface salinity boundary condition in the OGCM is the combination of new well-posed boundary conditions (Jin et al., 2017) and restoring boundary conditions. This well-posed boundary condition uses the virtual salt flux that includes the proper correlations between the freshwater flux Fw and sea surface salinity, and the real salt flux is generally parameterized through 10-m wind speed U_{10}, which can conserve total ocean salinity, the details can be found in Jin et al. (2017). Here, the sea-ice concentration is prescribed by its observed value from the National Snow and Ice Data Center (NSIDC) (Walsh et al., 2015).

The CGCM is the current version of the Chinese Academy of Sciences' Earth System Model (CAS-ESM), which consists of IAP4.0 (Zhang et al., 2013) for the atmosphere, revised LICOM2.0 for the ocean, CoLM ((Dai et al.,

2004; Ji et al., 2014) for the land surface, and CICE4.0 (Hunke and Lipscomb, 2008) for sea ice. The atmospheric model uses a finite-difference scheme with a terrain-following coordinate and a latitude–longitude grid with a horizontal resolution of 1.4° × 1.4°. Arakawa's staggered C grid is used for horizontal discretization. Furthermore, the top of the atmospheric model is about 2.2 hPa, and there are 30 layers in the vertical. CoLM and CICE4.0 share the same horizontal grid as the atmospheric and ocean models, respectively. The ecosystem and chemistry of CAS-ESM are closed in our study. A series of CAS-ESM versions (including its predecessor and component models) have been widely adopted in previous studies and applications, including, atmospheric circulation in middle-to-high latitudes (Dong et al., 2014), decadal variations of the East Asian summer monsoon (Dong and Xue, 2016; Lin et al., 2016), ENSO (Su et al., 2015), ocean assimilation in a coupled model framework (Dong et al., 2016, 2021b; Du et al., 2020), and short-term climate predictions for China (Lin et al., 2019). Although CAS-ESM is a newcomer in the community, since this is the first time that it is contributing to CMIP6 simulations, it has a good ability to reproduce the basic performances of the radiation budget of the atmosphere and ocean, precipitation, circulations, variabilities, the twentieth-century warming, and so on (Zhang et al., 2020).

2.2. *Experiments*

We designed two groups of experiments, one used the stand-alone revised LICOM2.0, and the other used CAS-ESM. Each group included two experiments, one control and one perturbation experiment. For the control experiments, the OGCM and CGCM was spun up to reach a quasi-equilibrium state. For the OGCM, the Coordinated Ocean-ice Reference Experiments-I (CORE I) protocol proposed by Griffies et al. (2009) was employed, the repeating annual cycle of atmospheric forcing from Large and Yeager (2004) was used, and the model was spun up for 300 years. For the CGCM, the model was integrated for 1000 years under the pre-industrial scenario. Two additional 100-year simulations for both the coupled and uncoupled models were conducted by using the spin-up experiments as initial conditions. The OGCM and CGCM experiments are called OCTRL and CCTRL, respectively, and are listed in Table 1.

For the two perturbation simulations, both experiments started from the quasi-equilibrium state of the spin-up experiments, but the prescribed surface heat flux perturbation (F) of FAFMIP was bilinearly interpolated onto the OGCM's native grid and added to the sea surface heat flux which was used to calculate the temperature equation, which is from one of the FAFMIP experiments (denoted by FAF-heat in FAFMIP). Bilinear interpolation has been adopted in FAFMIP experiments (Todd et al., 2020). F was not directly applied to the sea-ice heat budget in order to eliminate the effects of sea ice. The turbulent heat fluxes for both the OGCM and CGCM were computed using the same bulk formulae. All other settings were the same as their control runs. We refer to the two OGCM and CGCM perturbation experiments as "OExp1" and "CExp1" in Table 1, respectively. To calculate the mean values for the basins, the ocean was divided into three parts: the Indo-Pacific Ocean (IP, 22°–134°E and 35°S–65°N), the Arctic and Atlantic Ocean (AA, 35°S–90°N). and the Southern Ocean (SO, 78°S–35°N).

2.3. *Passive tracer method*

Here, the passive tracer approach recommended by FAFMIP was adopted to separate the contributions of changes in ocean circulation and anomalous surface heat flux from temperature (Gregory et al., 2016). This method divides the temperature change into the added and redistributed components in the perturbation experiments.

In the following, the subscripts "c" and "p" denote values in the control and perturbation experiments, respectively, and primes denote the difference between the perturbation experiment and the control. The temperature equation for the control experiment can be schematically expressed as follows:

$$\frac{\partial T_c}{\partial t} = -\nabla \cdot (v_c T_c) + Q_c \,. \tag{1}$$

The equation sets the volumetric heat capacity to unity for convenience. Q_c is the surface heat flux and applies only to the ocean surface, and $\nabla \cdot (v_c T_c)$represents all heat transport processes in the ocean, including large-scale and eddy-induced advection, diffusion due to sub-grid processes and deep convection, etc.

For perturbation experiments, the corresponding equa-

Table 1. The configurations and the global mean values of ocean temperature anomaly (T'), the added temperature change (T'_a), and the redistributive temperature anomaly (T'_r) for all OGCM and CGCM experiments, as well as changes in the maximum AMOC transport.

Experiments	Models	Surface heat flux perturbation	Global mean T' (the 100th yr, K)	Global mean T'_a (the 100th yr, K)	Global mean T'_r (the 100th yr, K)	The change in maximum AMOC (Sv)
OCTRL	LICOM2.0	0	–	–	–	–
OExp1	LICOM2.0	$F + Q'_t$	0.443	0.386	0.057	7.27
CCTRL	CAS-ESM	0	–	–	–	–
CExp1	CAS-ESM	$F + Q'_t$	0.419	0.371	0.048	8.52

tion for the temperature change with the addition of heat flux (F) and atmosphere–ocean heat flux Q_p is as follows:

$$\frac{\partial T_p}{\partial t} = -\nabla\cdot\left(v_p T_p\right) + Q_p + F\,, \tag{2}$$

where $\nabla\cdot\left(v_p T_p\right)$ differs from $\nabla\cdot(v_c T_c)$ because the velocities and diffusivities are changed due to the effects of F, and T_p affecting seawater density. The critical difference from the control experiment is that the SST for computing Q_p is supplied by a passive tracer T_r, described below, instead of T_p.

A passive tracer T_r is introduced and used to calculate Q_p in order to maximize the effect of F on the sea surface. T_r is not forced by the heat flux perturbation F and is only affected by changes in velocities and diffusivities due to the effects of F. The seawater density is computed using T_p instead of T_r, which means that the change in T_r cannot affect ocean circulation. The equation for the passive tracer T_r is as follows:

$$\frac{\partial T_r}{\partial t} = -\nabla\cdot\left(v_p T_r\right) + Q_p\,, \tag{3}$$

T_p and T_r are both initialized to T_c, so we can write $T_p = T_c + T'$ and $T_r = T_c + T'_r$. Q_p and v_p are split into $Q_c + Q'_r$ and $v_p = v_c + v'$, respectively.

According to the above decomposition, the equation for the temperature anomaly can be derived through Eqs. (1) and (2) as follows:

$$\frac{\partial T'}{\partial t} = -\nabla\cdot\left(v_c T' + v' T_c + v' T'\right) + F + Q'_r\,. \tag{4}$$

The difference between T_c and T_r is the temperature anomaly due to the circulation change v' and redistributed heat flux anomaly Q'_r, which is defined as the redistributive temperature anomaly T'_r. T'_r can be derived according to Eq. (3) – Eq. (1):

$$\frac{\partial T'_r}{\partial t} = -\nabla\cdot\left(v_c T'_r + v' T_c + v' T'_r\right) + Q'_r\,. \tag{5}$$

According to previous studies (Garuba and Klinger, 2016, 2018), we can attribute the added temperature anomaly (T'_a) to the absorption of the prescribed perturbation in surface heat flux F, which can be obtained by Eqs. (4) – (5). The corresponding equation is as follows:

$$\frac{\partial T'_a}{\partial t} = -\nabla\cdot\left(v_c T'_a + v' T'_a\right) + F\,. \tag{6}$$

Thus, the redistributive temperature perturbation T'_r mainly results from both the redistributed transport term ($v'T_c$) due to the circulation change and the initial current (or background current) transport term ($v_c T'_r$) due to the redistributive temperature change on the right side of Eq. (5). The added heat anomaly mainly results from the initial current transport term ($v_c T'_a$) due to added heat temperature change on the right side of Eq. (6). The total temperature anomaly can be regarded as the sum of the redistributive temperature anomaly (T'_r) and the added heat anomaly (T'_a), which are the focus of the present study.

3. Results

The surface heat flux perturbation plays a predominant role in the weakening of the AMOC and increases the OHU among surface flux perturbations (Rahmstorf and Ganapolski, 1999; Gregory et al., 2005, 2016; Bouttes and Gregory, 2014). Figure 1 shows the patterns of the prescribed surface heat flux anomaly F and the redistributed heat flux anomaly Q'_r during the final decade of both the OGCM and CGCM. The evident heating of the surface heat flux anomaly F primarily occurs in the North Atlantic and the SO (Figs. 1a and 1c). The values of F are almost identical between the OGCM and CGCM, and the ocean areal mean F in both simulations are 1.87 W m^{-2} and 1.81 W m^{-2}, which is consistent with the value (1.86 W m^{-2}) provided by Gregory et al. (2016). In the OGCM, F exhibits slightly more heat input in the Labrador Sea and Bering Strait (Fig. 1e), which is caused by a greater concentration of sea ice in the OGCM compared to that in the CGCM. The sea ice concentration in the OGCM is a prescribed observation and uses simulated values by the sea-ice model CICE4.0 in the CGCM.

A predominant feature of Q'_r in both simulations is that it is relatively large and positive in the North Atlantic and negative in the low latitudes of the Atlantic (Figs. 1b and 1d), which is related to the weakening of the AMOC due to the heat flux perturbation, F. Due to strong positive feedback, the AMOC weakening leads to the cooling of redistributed sea surface temperature (SSTr), the freshening of the sea surface salinity in the North Atlantic, and SSTr warming in the low latitudes of the Atlantic due to a reduced northward transport of warm and salty water, which enhances the local heat input to the North Atlantic and further exaggerates the weakening of the AMOC.

The difference in Q'_r between the OGCM and CGCM is mainly observed in the Atlantic, SO, and the Kuroshio region. Q'_r in the OGCM exhibited less heat input in the North Atlantic, which is a result of the decreased weakening of the AMOC relative to the CGCM. In this region (red box of Fig. 1a), the average values of Q'_r are 14.3 W m^{-2} and 19.5 W m^{-2} in the OGCM and CGCM, respectively. The corresponding mean of F in this region is 10.7 W m^{-2}, so the average values of Q'_r and F in this region are nearly equal, which means that the effect of F is similar and even less than that of Q'_r. For the SO, the simulated Q'_r is lower in the OGCM compared to the CGCM because the shortwave flux is prescribed in the former and simulated by the atmospheric model in the latter [Fig. S1 in the electronic supplementary material (ESM)].

The simulated AMOC, ocean heat content, and sea-level change which are essential measures in predicting

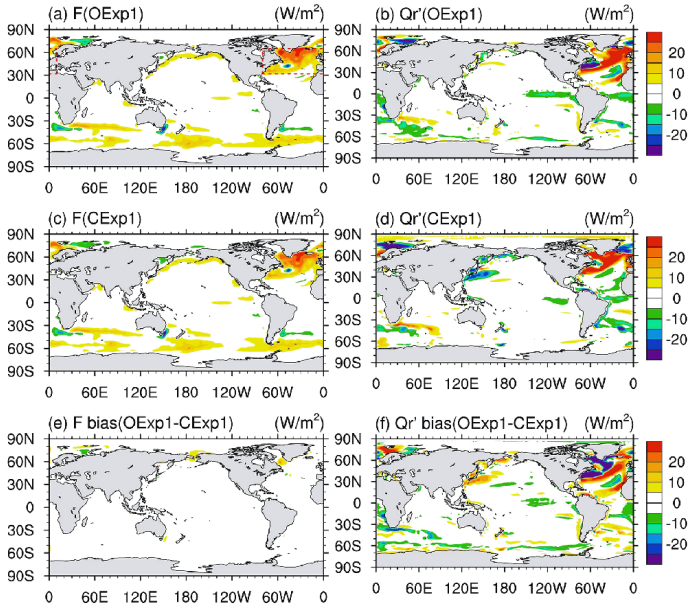

Fig. 1. The prescribed heat flux anomaly (F) from FAFMIP for (a) OExp1, (c) CExp1, and (e) their differences (OExp1 – CExp1). (b), (d), (f), describe the same results as (a), (c), (e), but for the heat flux anomaly due to the redistribution of the SST (Q_r') (units: W m^{-2}), the positive value indicates downward.

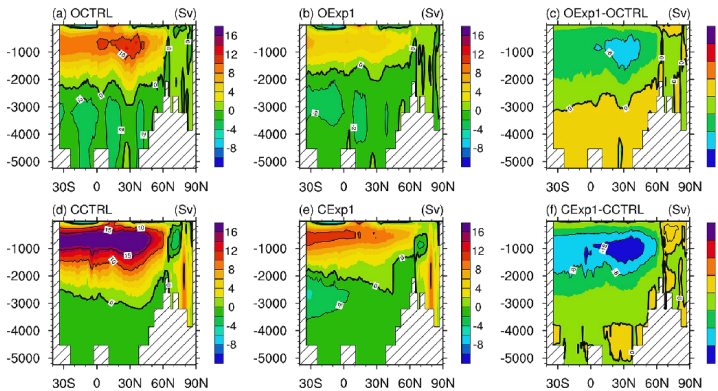

Fig. 2. The Atlantic Meridional Overturning Circulation (AMOC) for the OGCM (a) control run (OCTRL), (b) perturbation run (OExp1), and (c) their difference (OExp1 – OCTRL). (d), (e), (f), show the same results as (a), (b), (c), but for CGCM (units: Sv).

future climate change, are discussed in the following. The prescribed heat flux perturbation, F, into the Atlantic mainly occurs in the North Atlantic region, which enhances the ocean stratification stability, and the subsequent reduction in subduction results in the weakening of AMOC. Figure 2 shows the AMOC and its changes for the OGCM and CGCM. In both the OGCM and CGCM, the AMOC declines in response to the imposed heat flux anomaly, F. Compared with the OGCM, the stronger initial AMOC and larger reduction in transport due to warming in the coupled model leads to greater cooling in the Atlantic (Fig. 2, Winton et al., 2013), which can explain the difference in the redistributed heat flux anomaly Q_r' in the AA between the OGCM and CGCM. The corresponding maximum values of the AMOC simulated in the CCTRL and OCTRL are 19.7 Sv and 13.2 Sv, respectively, while changes in the maximum AMOC for the OGCM and CGCM are 7.3 Sv and 8.5 Sv (Figs. 2c and 2f). The larger reduction in the AMOC in the CGCM is consistent with the results of Todd et al. (2020). This difference is largely due to lower salinity in the North Atlantic in the CGCM relative to that in the OGCM (Fig. S2) since the OGCM combines the restoring and well-posed salinity boundary conditions, and the CGCM only uses the well-posed salinity boundary condition.

Figure 3 shows the spatial distribution of the total OHC change ($\int_{-H}^{0}\rho_0 c_p T'\mathrm{d}z$), the change in added OHC ($\Delta\mathrm{OHCa}, \int_{0}^{-H}\rho_0 c_p T_a'\mathrm{d}z$) and the change in redistributed OHC ($\Delta\mathrm{OHCr}, \int_{0}^{-H}\rho_0 c_p T_r'\mathrm{d}z$) for the OGCM and CGCM, as well as their differences (OGCM – CGCM). The changes in total OHC are mainly determined by the change in added OHC, especially for the Atlantic and Southern Oceans. The spatial pattern and magnitude of vertically integrated changes in the added heat are very similar between the two models, and the increased OHC in FAF-heat is primarily determined by ΔOHCa, especially for the Atlantic and Southern Oceans. It is noted that the redistributed OHC change is also important for determining the geographical pattern of the OHC change, such as in the North Atlantic, western boundary currents, and high latitudes (Figs. 3a–f).

The large discrepancies between the OGCM and CGCM occurring in the AA basin are also due to the redistributed temperature T_r' (Figs. 3g–i), as reflected in the basin mean values and OHU. The large positive values can be found in the Gulf Stream region and South Atlantic. Compared with the OGCM, the stronger initial AMOC and larger reduction in transport in the coupled model leads to stronger cooling in the Atlantic (Fig. 4, Winton et al., 2013). This can explain the difference in the redistributed heat flux anomaly in the AA between the OGCM and CGCM.

Long-term variations are fundamental metrics for assessing the performance of the model. Figure 4 shows the time series of the mean ocean temperature anomaly T', T_a' and T_r' at the global and basin scales simulated by both the OGCM and CGCM. The temperature changes show a similar linear rising trend in both experiments. The warming trends are mainly caused by the added heat anomaly T_a', which contributes to approximately 90% of the increase in T', while the contribution of T_r' is about 10%.

The global mean temperature change T' for the OGCM

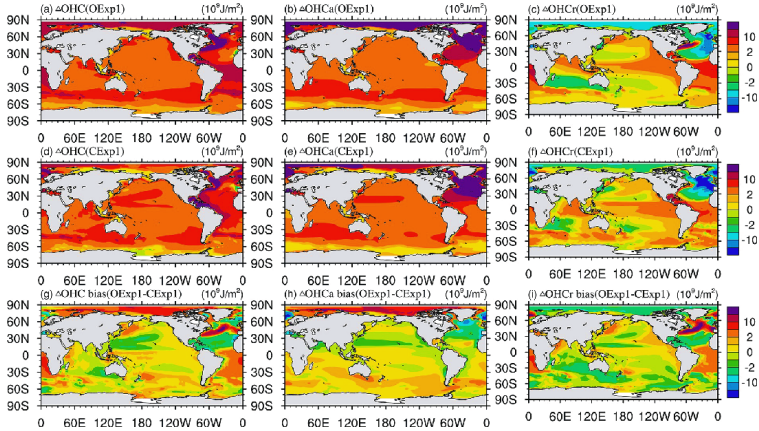

Fig. 3. The total ocean heat content change due to (a) the ocean temperature anomaly (T), (b) added temperature change (T_a'), and (c) the redistributive temperature anomaly (T_r') during the final decade of the experiments for OGCM. (d,) (e), (f), show the same results as (a), (b), (c), but for CGCM. (g), (h), (i), are the differences in T', T_a', and T_r' between the OGCM and CGCM, respectively (units: 10^9 J m^{-2}).

is about 5% greater than that for the CGCM (Fig. 4a). The values of global mean T' in the 100th year for the OGCM and CGCM are 0.443°C and 0.419°C, respectively (Table 1). The added and redistributed heat tracers both have positive contributions to the difference in T' between the OGCM and CGCM (Fig. 4a): 0.015°C (0.386°C – 0.371°C) and 0.009°C (0.057°C – 0.048°C), respectively (Table 1). Similar to the temperature change, the OHU (24.1×10^{23} J, $\int \rho_0 c_p T' dV$) in the OGCM is also slightly larger than that (22.8×10^{23} J) in the CGCM (Table 2). In general, the differences in T' and OHU between the two models are attributed more to F and Q'_r in the OGCM than those in the CGCM (Fig. 5a). The heat inputs of F and Q'_r are 21.0×10^{23} J and 3.1×10^{23} J in the OGCM and 20.2×10^{23} J and 2.6×10^{23} J in the CGCM, respectively (Table 2). In addition, the magnitude of interannual variability in surface heat fluxes for the CGCM is much larger than that for the OGCM due to the stronger intrinsic variability, but we do not discuss this issue here.

The basin mean values of T',T'_a, and T'_r for the OGCM and CGCM further show that the differences in T' between the two models mainly occur in the AA and SO basins, while they are much smaller in the IP basin (Figs. 4b–d). The AA basin mean T' in the 100th year in the OGCM is larger than that in the CGCM, which is mainly caused by the difference in T'_r. The corresponding average values of OHU in the 100th year in the OGCM and CGCM are 8.4×10^{23} J and 7.2×10^{23} J, respectively. The redistributed OHU (OHUr) ($\int \rho_0 c_p T'_r dV$) in the OGCM is 0.4×10^{23} J, which is significantly larger than that in the CGCM (-0.9×10^{23} J) (Table 2). This is mainly attributed to the decreased change in southward meridional heat transport for T'_r [the main contributor to the $v'T_c$ term; see Eq. (5)] from the AA to the SO in the OGCM (-3.4×10^{23} J) relative to that in the CGCM (-6.2×10^{23} J), which, in turn, is because the redistributed heat flux anomaly input (3.9×10^{23} J) in the OGCM is less than that (5.5×10^{23} J) in the CGCM due to the greater weakening of the AMOC simulated in the CGCM (Fig. 2). The larger weakening of AMOC mainly resulted from lower salinity in the North Atlantic in the CGCM relative to that in the OGCM (Fig. S2 in the ESM). The T'_a of the AA basin is

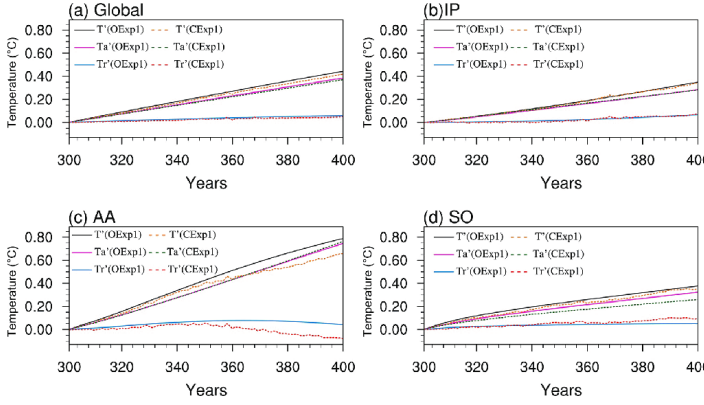

Fig. 4. The global and basin mean changes in ocean temperature anomaly (T), added temperature change (T'_a), and redistributive temperature anomaly (T'_r) simulated by the OGCM and CGCM for (a) global, (b) the Indo-Pacific (IP), (c) the Arctic-Atlantic (AA), and (d) Southern (SO) Oceans (units: °C).

Table 2. Time-integrated total surface heat flux anomaly ($F + Q'_r$), prescribed heat flux anomaly (F), redistributed heat flux anomaly (Q'_r), and OHU ($\int \rho_0 c_p T' dV$), added OHUa ($\int \rho_0 c_p T'_a dV$) and redistributed OHUr ($\int \rho_0 c_p T'_r dV$) in the OGCM and CGCM experiments.

	OGCM (10^{23} J)				CGCM (10^{23} J)			
	Global	Atl-Arc	Pac-Ind	Southern	Global	Atl-Arc	Pac-Ind	Southern
OHU	24.1	8.4	10.4	5.3	22.8	7.2	10.6	5.0
OHUa	21.0	8.0	8.4	4.6	20.2	8.1	8.4	3.7
OHUr	3.1	0.4	2.0	0.7	2.6	–0.9	2.2	1.3
$\int (F + Q'_r) dA$	24.1	10.5	4.6	9.0	22.8	11.5	2.8	8.5
$\int F dA$	21.0	6.6	5.6	8.8	20.2	6.0	5.5	8.7
$\int Q'_r dA$	3.1	3.9	–1.0	0.2	2.6	5.5	–2.7	–0.2

almost the same between the two experiments. For the SO, the added OHU (OHUa) ($\int \rho_0 c_p T'_a dV$) in the OGCM is 0.9 × 10^{23} J more than that in the CGCM, while the OHUr in the OGCM is 0.6 × 10^{23} J less than that in the CGCM. Therefore, the differences in the two terms almost cancel out and lead to a greater increase (albeit slight) in OHU in the OGCM compared to the CGCM. This further indicates that the redistributive effect plays an important role in OHU in the AA and SO basins.

The basin heat flux anomaly input and the tendency of OHU are not balanced, which is mainly because of the heat exchange between the basins, especially between the AA and SO. For instance, in the SO, the prescribed heat flux, F, in the OGCM is almost the same as that in the CGCM, and the redistributed heat Q'_r input (0.2 × 10^{23} J) in the OGCM is larger than that (–0.9 × 10^{23} J) in the CGCM (Fig. 5d and Table 2). The basin mean T'_a and OHUa for the SO in the OGCM is larger than that in the CGCM, and the basin mean T'_r and OHUr in the OGCM are less than that in the CGCM (Fig. 4d and Table 2). The former is mainly related to a greater change in northward meridional heat transport for T'_a (the main contributor to the $v_c T'_a$ term; see Eq. 6) in the CGCM (2.0 × 10^{23} J) than that in the OGCM (1.3 × 10^{23} J), which is due to the larger initial strength of the AMOC in the CCTRL (Fig. 2d), and the latter is largely a result of a greater change in southward meridional heat transport from the AA to SO in the CGCM (main contributor to the $v'T_c$ term) due to a larger reduction in the AMOC (Table 3).

We further examined the effects of thermal expansion on sea-level rise. Here, the spatial distribution of the changes in the SSL [steric sea level, $\int_0^{-H} \rho(T,S) - \rho(T_0,S_0)/\rho(T_0,S_0)\,dz$], the TSSL [thermosteric sea level, $\int_0^{-H} \rho(T,S_0) - \rho(T_0,S_0)/\rho(T_0,S_0)\,dz$], and the HSSL [halosteric sea level, $\int_0^{-H} \rho(T_0,S) - \rho(T_0,S_0)/\rho(T_0,S_0)\,dz$] for the OGCM and CGCM, as well as their differences, are shown in Fig. 6. Similar to the spatial pattern of changes in the vertically integrated OHC, the spatial patterns of changes in SSL, TSSL, and HSSL are also almost similar between the two models. The changes in SSL in both models are mainly determined by the change in TSSL. HSSL is of regional importance in the AA and SO basins. Compared to the CGCM, a larger rise in TSSL in the OGCM is observed in the Gulf Stream region and South Atlantic, which are similar to the differ-

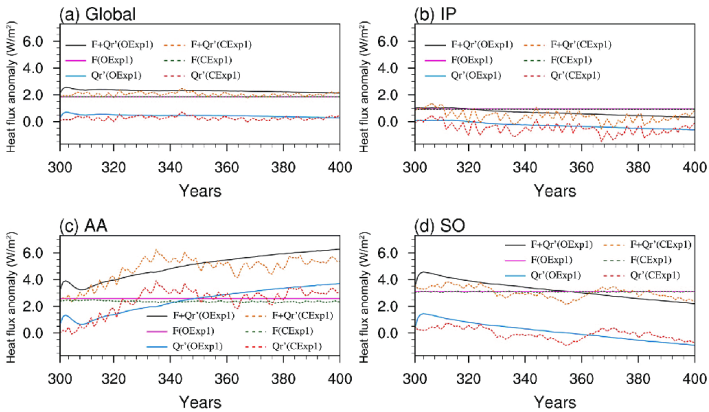

Fig. 5. The global and the basin means time series of the heat flux anomaly (F) from FAFMIP, the heat flux anomaly (Q'_r) resulting from the redistribution of SST and the total surface heat flux anomaly ($F + Q'_r$) simulated by the OGCM and CGCM for the (a) global, (b) the Indo-Pacific (IP), (c) the Arctic-Atlantic (AA), and (d) the Southern (SO) Oceans (units: W m^{-2}).

Table 3. Time-integrated meridional heat transport of total temperature change (T'), redistributed temperature change (T'_r), and added temperature change (T'_a) simulated by the OGCM and CGCM. A positive value denotes northward meridional heat transport (MHT).

	OGCM (10^{23} J)			CGCM (10^{23} J)		
Basin	T'	T'_r	T'_a	T'	T'_r	T'_a
SO-AA	–2.1	–3.4	1.3	–4.2	–6.2	2.0
IP-AA	0.03	–0.1	0.1	–0.1	–0.2	0.1
IP-SO	5.8	2.9	2.9	7.7	4.7	3.0

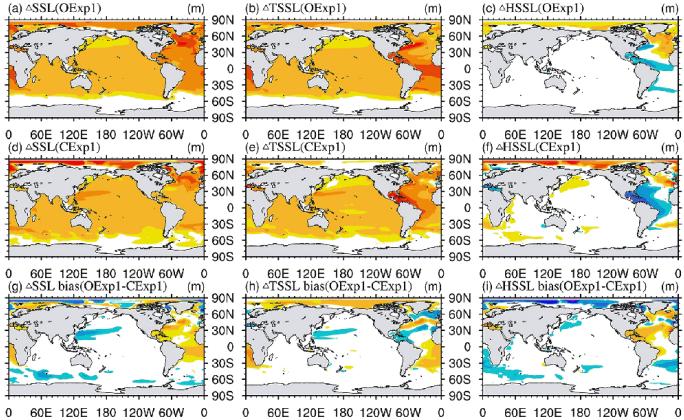

Fig. 6. The spatial distribution of changes in SSL [steric sea level, $\int_0^{-H}\rho(T,S)-\rho(T_0,S_0)/\rho(T_0,S_0)\mathrm{d}z$] for (a) OGCM, (d) CGCM, and (g) their differences (OGCM – CGCM); (b), (e), (h), and (c), (f), (i), show the same results as (a), (d), (g), but for TSSL [thermosteric sea level, $\int_0^{-H}\rho(T,S_0)-\rho(T_0,S_0)/\rho(T_0,S_0)\mathrm{d}z$)] and HSSL [halosteric sea level, $\int_0^{-H}\rho(T_0,S)-\rho(T_0,S_0)/\rho(T_0,S_0)\mathrm{d}z$](units: m).

ence in the vertically integrated OHC change between the two models. The discrepancies between the OGCM and CGCM occur in the AA and SO basins due to the combined effects of TSSL and HSSL (Figs. 6g–i). The difference in HSSL in the Arctic Ocean and SO between the OGCM and CGCM are also mainly due to the different sea salinity boundary conditions between the two models.

4. Summary and discussion

In this study, the differences in the simulated response to global warming between a stand-alone ocean model and a fully-coupled model were investigated using heat flux anomaly experiments according to the FAFMIP protocol (Gregory et al., 2016). We found that global mean warming trends are mainly caused by anomalous surface heating (F) which contributes approximately 90% to the increase in T'. An important finding is that the global mean temperature changes (T', T'_r and T'_a), ocean heat content changes (OHU, OHUa, and OHUr), and the spatial patterns of SSL and TSSL changes are generally consistent between the stand-alone OGCM and CGCM simulations, indicating that the ocean model alone can also be used to approximate ocean heat uptake processes and changes in SSL.

This study also reveals slight differences in ocean climate changes between the OGCM and CGCM. For the global mean variables, the magnitudes of the global temperature change T' and OHU in the OGCM are about 5% greater than those in the CGCM, which is the result of the combined effect of the added temperature change T'_a due to the added heat flux perturbation (F) and the redistributed temperature change T'_r due to the redistributed heat flux anomaly Q'_r. A larger weakening of the AMOC occurred in the CGCM which was largely attributed to lower salinity values in the North Atlantic relative to that in the OGCM, this is because the restoring salinity boundary condition is applied in the OGCM and absent in the CGCM. Consistent with previous studies (Gregory et al., 2016), we found that the greater AMOC weakening in coupled models causes an increased input from the redistributed heat flux anomaly Q'_r in the AA region compared to stand-alone models. However, the global mean Q'_r in the coupled model is lower than that in the OGCM; this difference is attributed to a lack of air–sea interaction in the OGCM because the shortwave flux and surface air temperature are prescribed in the stand-alone model and simulated by AGCM in the CGCM (Fig. S1 in the ESM).

For the basin-scale results, we find that for the IP basin, the mean temperature and ocean heat content changes in the OGCM are almost identical to those in the CGCM. In contrast, there is a warmer basin mean temperature change T' and a larger OHU in the SO and AA in the OGCM relative to those in the CGCM. The smaller changes in added heat temperature T'_a and the OHUa of the SO in the CGCM are largely due to the initial greater strength of the AMOC, which exhibits a greater northward meridional heat transport for T'_a from the SO to AA. The differences in T'_r in the SO and AA between the two models are mainly due to the different degrees of weakening of the AMOC in response to global warming. Since the greater weakening of the AMOC

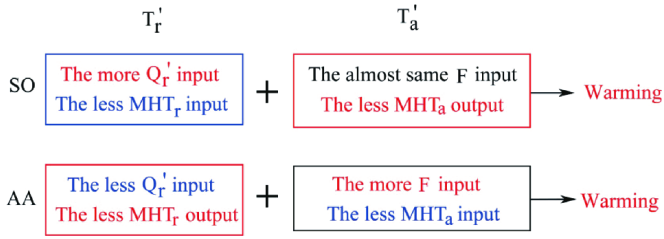

Fig. 7. Diagram describing the difference in T' (corresponding to OHU), T'_a (corresponding to OHUa), and T'_r (corresponding to OHUr) between the OGCM and CGCM. The figures show whether they exhibit warming (red) or cooling (blue) in the OGCM compared to CGCM. MHTa is the northward meridional heat transport for T'_a, and MHTr is the northward meridional heat transport for T'_r.

is accompanied by a larger North Atlantic SST cooling in a CGCM, it will have the effect of not only amplifying the Q'_r input relative to the OGCM (especially for the North Atlantic) but will also provide for a greater southward meridional heat transport change from the AA to the SO. Besides, the atmosphere–ocean feedbacks that are present in CGCM and absent in OGCM tend to enhance the pattern of the North Atlantic OHC and TSSL changes, exhibiting relatively stronger increases in the tropics and decreases in the extratropics. The above processes are schematically described in Fig. 7.

Both the CGCM and OGCM show that the SSL is mainly determined by the change in TSSL. Changes in the TSSL and HSSL largely cancel out, but both terms contribute to the overall SSL change in the SO and AA basins. The main discrepancies in SSL between the CGCM and OGCM over the Atlantic and SO are due to differences in the HSSL change, which are also related to the difference in sea surface salinity boundary conditions between the models.

The SO is a key region for the absorption and storage of anthropogenic heat. This study only focused on the effects of F regarding ocean climate change. While the SO ocean heat uptake is also closely related to the magnitudes of the wind and gyre boundary poleward shifts (Sen Gupta et al., 2009; Lyu et al., 2020), it is worth investigating what role the wind stress change plays in the ocean heat uptake and redistribution by analyzing wind stress perturbation experiments (FAF-stress) in FAFMIP.

In this study, we only compared the output from the OGCM and CGCM using one Earth system model (CAS-ESM2) and its ocean component. Although the differences between the OGCM and CGCM are explained reasonably well, we cannot confirm whether the results are model dependent. FAFMIP provides an opportunity to investigate inter-model differences, such as Todd et al. (2020) who examined the ocean's response (especially for ocean heat uptake and dynamic sea-level change) to surface momentum and buoyancy flux perturbations provided by FAFMIP in an ensemble of five OGCMs and two CGCMs. Besides, more physical meaning should be considered, for instance, if climate models have a initially cold bias over the SO and are also accompanied by an eddy-driven jet equatorward bias in the mid-latitudes, and more cloud cover and sea ice, which tends to enhance the effects of global warming (Kajtar et al., 2021).

Finally, adopting method B of FAFMIP will result in the same order of magnitude for the calculated Q'_r and the prescribed heat flux perturbation F, in the North Atlantic, which means that the effect of F is accounted for twice, resulting in a further reduction in AMOC intensity compared to the scenario of doubled CO_2 concentration. Currently, to eliminate the effects of the doubled contribution of F, FAFMIP has provided a new experiment, in which the added heat flux perturbation F, is multiplied by 0.5 for part of the North Atlantic. The results of the new experiment and the calculation of heat flux in high-latitude regions in the North Atlantic remain issues that are worthy of investigation in the future.

Acknowledgements. The constructive suggestions and comments from the two anonymous reviewers and Editor are highly appreciated. This work is jointly supported by the Strategic Priority Research Program of the Chinese Academy of Sciences (Grant No. XDA19020202), Key Research Program of Frontier Sciences, the Chinese Academy of Sciences (Grant No. ZDBS-LY-DQC010), the Strategic Priority Research Program of the Chinese Academy of Sciences (Grant No. XDB42000000) and the open fund of State Key Laboratory of Satellite Ocean Environment Dynamics, Second Institute of Oceanography (Grant No. QNHX2017). Xiao DONG was supported by the National Natural Science Foundation of China (Grant No. 41706028). The simulations were performed on the supercomputers provided by Earth System Science Numerical Simulator Facility (EarthLab).

Electronic supplementary material: Supplementary material is available in the online version of this article at https://doi.org/10.1007/s00376-021-1167-y.

REFERENCES

Bouttes, N., and J. M. Gregory, 2014: Attribution of the spatial pattern of CO_2-forced sea level change to ocean surface flux changes. *Environmental Research Letters*, **9**, 034004, https://doi.org/10.1088/1748-9326/9/3/034004.

Canuto, V. M., A. Howard, Y. Cheng, and M. S. Dubovikov, 2001: Ocean turbulence. Part I: One-point closure model-momentum and heat vertical diffusivities. *J. Phys. Oceanogr.*, **31**, 1413–1426, https://doi.org/10.1175/1520-0485(2001)031<1413:OTPIOP>2.0.CO;2.

Canuto, V. M., A. Howard, Y. Cheng, and M. S. Dubovikov, 2002: Ocean turbulence. Part II: Vertical diffusivities of momentum, heat, salt, mass, and passive scalars. *J. Phys. Oceanogr*, **32**, 240–264, https://doi.org/10.1175/1520-0485(2002)032<0240:OTPIVD>2.0.CO;2.

Church, J. A., N. White, C. M. Domingues, D. P. Monselesan, and E. R. Miles, 2013: Sea-level and ocean heat-content change. *International Geophysics*, **103**, 697–725, https://doi.org/10.1016/B978-0-12-391851-2.00027-1.

Dai, Y. J., R. E. Dickinson, and Y. P. Wang, 2004: A two-big-leaf model for canopy temperature, photosynthesis, and stomatal conductance. *J. Climate*, **17**, 2281–2299, https://doi.org/10.1175/1520-0442(2004)017<2281:ATMFCT>2.0.CO;2.

Dong, X., and F. Xue, 2016: Phase transition of the pacific decadal oscillation and decadal variation of the East Asian summer monsoon in the 20th century. *Adv. Atmos. Sci.*, **33**(3), 330–338, https://doi.org/10.1007/s00376-015-5130-7.

Dong, X., T. H. Su, J. Wang, and R. P. Lin, 2014: Decadal variation of the Aleutian Low-Icelandic Low seesaw simulated by a climate system model (CAS-ESM-C). *Atmos. Ocean. Sci. Lett.*, **7**(2), 110–114, https://doi.org/10.3878/j.issn.1674-2834.13.0061.

Dong, X., R. P. Lin, J. Zhu, and Z. T. Lu, 2016: Evaluation of ocean data assimilation in CAS-ESM-C: Constraining the SST field. *Adv. Atmos. Sci.*, **33**, 795–807, https://doi.org/10.1007/s00376-016-5234-8.

Dong, X., and Coauthors, 2021a: CAS-ESM2.0 model datasets for the CMIP6 Ocean Model Intercomparison Project Phase 1 (OMIP1). *Adv. Atmos. Sci.*, **38**(2), 307–316, https://doi.org/10.1007/s00376-020-0150-3.

Dong, X., F. Zheng, R. P. Lin, H. P. Yang, J. Zhu, M. J. Du, and H. Luo, 2021b: A reasonable mean dynamic topography state on improving the ability of assimilating the altimetry observations into a coupled climate system model: An example with CAS-ESM-C. *J. Geophys. Res.*, **126**(2), e2020JC016760, https://doi.org/10.1029/2020JC016760.

Du, M. J., F. Zheng, J. Zhu, R. P. Lin, H. P. Yang, and Q. L. Chen, 2020: A new ensemble-based approach to correct the systematic ocean temperature bias of CAS-ESM-C to improve its simulation and data assimilation abilities. *J. Geophys. Res.*, **125**, e2020JC016406, https://doi.org/10.1029/2020JC016406.

Garuba, O. A., and B. A. Klinger, 2016: Ocean heat uptake and inter-basin transport of passive and redistributive surface heating. *J. Climate*, **29**, 7507–7527, https://doi.org/10.1175/JCLI-D-16-0138.1.

Garuba, O. A., and B. A. Klinger, 2018: The role of individual surface flux components in the passive and active ocean heat uptake. *J. Climate*, **31**, 6157–6173, https://doi.org/10.1175/JCLI-D-17-0452.1.

Gent, P. R., and J. C. McWilliams, 1990: Isopycnal mixing in ocean circulation models. *J. Phys. Oceanogr.*, **20**, 150–155, https://doi.org/10.1175/1520-0485(1990)020<0150:IMIOCM>2.0.CO;2.

Gregory, J. M., and Coauthors, 2005: A model intercomparison of changes in the Atlantic thermohaline circulation in response to increasing atmospheric CO_2 concentration. *Geophys. Res. Lett.*, **32**, L12703, https://doi.org/10.1029/2005GL023209.

Gregory, J. M., and Coauthors, 2016: The Flux-Anomaly-Forced Model Intercomparison Project (FAFMIP) contribution to CMIP6: Investigation of sea-level and ocean climate change in response to CO_2 forcing. *Geoscientific Model Development*, **9**, 3993–4017, https://doi.org/10.5194/gmd-9-3993-2016.

Griffies, S. M., and Coauthors, 2009: Coordinated ocean-ice reference experiments (COREs). *Ocean Modelling*, **26**(1-2), 1–46, https://doi.org/10.1016/j.ocemod.2008.08.007.

Huber, M. B., and L. Zanna, 2017: Drivers of uncertainty in simulated ocean circulation and heat uptake. *Geophys. Res. Lett.*, **44**, 1402–1413, https://doi.org/10.1002/2016GL071587.

Hunke, E. C., and W. H. Lipscomb, 2008: CICE: The Los Alamos sea ice model documentation and software user's manual, version 4. *0. Los Alamos National Laboratory Tech. Rep. LA-CC-06-012*, 76pp.

Ji, D., and Coauthors, 2014: Description and basic evaluation of Beijing Normal University Earth System Model (BNU-ESM) version 1. *Geoscientific Model Development*, **7**, 2039–2064, https://doi.org/10.5194/gmd-7-2039-2014.

Jin, J. B., and Coauthors, 2021: CAS-ESM2.0 model datasets for the CMIP6 Flux-Anomaly-Forced Model Intercomparison Project (FAFMIP). *Adv. Atmos. Sci.*, **38**(2), 296–306, https://doi.org/10.1007/s00376-020-0188-2.

Jin, J. B., Q. C. Zeng, L. Wu, H. L. Liu, and M. H. Zhang, 2017: Formulation of a new ocean salinity boundary condition and impact on the simulated climate of an oceanic general circulation model. *Science China Earth Sciences*, **60**, 491–500, https://doi.org/10.1007/s11430-016-9004-4.

Kajtar, J. B., A. Santoso, M. Collins, A. S. Taschetto, M. H. England, and L. M. Frankcombe, 2021: CMIP5 intermodel relationships in the baseline Southern Ocean climate system and with future projections. *Earth's Future*, **9**, e2020EF001873, https://doi.org/10.1029/2020EF001873.

Kuhlbrodt, T., and J. M. Gregory, 2012: Ocean heat uptake and its consequences for the magnitude of sea level rise and climate change. *Geophys. Res. Lett.*, **39**, L18608, https://doi.org/10.1029/2012GL052952.

Large, W. G., and S. G. Yeager, 2004: Diurnal to decadal global forcing for ocean and sea-ice models: The data sets and flux climatologies. NCAR/TN-460+STR, CGD Division of the National Center for Atmospheric Research, https://doi.org/10.5065/D6KK98Q6.

Lin, R. P., J. Zhu, and F. Zheng, 2016: Decadal shifts of East Asian summer monsoon in a climate model free of explicit GHGs and aerosols. *Scientific Reports*, **6**, 38546, https://doi.org/10.1038/srep38546.

Lin, R. P., J. Zhu, and F. Zheng, 2019: The application of the SVD method to reduce coupled model biases in seasonal predictions of rainfall. *J. Geophy. Res.*, **124**, 11837–11849, https://doi.org/10.1029/2018JD029927.

Liu, H. L., P. F. Lin, Y. Q. Yu, and X. H. Zhang, 2012: The baseline evaluation of LASG/IAP climate system ocean model (LICOM) version 2.0. *Acta Meteorologica Sinica*, **26**,

318–329, https://doi.org/10.1007/s13351-012-0305-y.

Lyu, K., X. B. Zhang, and J. A. Church, 2020: Regional dynamic sea level simulated in the CMIP5 and CMIP6 models: Mean biases, future projections, and their linkages. *J. Climate*, **33**(15), 6377–6398, https://doi.org/10.1175/JCLI-D-19-1029.1.

Marshall, J., K. C. Armour, J. R. Scott, Y. Kostov, U. Hausmann, D. Ferreira, T. G. Shepherd, and C. M. Bitz, 2014: The ocean's role in polar climate change: Asymmetric Arctic and Antarctic responses to greenhouse gas and ozone forcing. *Philosophical Transactions of the Royal Society A: Mathematical*, 372,20130040, https://doi.org/10.1098/rsta.2013.0040.

Pacanowski, R. C., 1995: MOM 2 Documentation, user's guide and reference manual. GFDL Ocean Tech. Rep. No.3, 232 pp.

Rahmstorf, S., and A. Ganapolski, 1999: Long-term global warming scenarios computed with an efficient coupled climate model. *Climatic Change*, **43**, 353–367, https://doi.org/10.1023/A:1005474526406.

Sen Gupta, A., A. Santoso, A. S. Taschetto, C. C. Ummenhofer, J. Trevena, and M. H. England, 2009: Projected changes to the southern hemisphere Ocean and sea ice in the IPCC AR4 climate models. *J. Climate*, **22**, 3047–3078, https://doi.org/10.1175/2008JCLI2827.1.

Su, T. H., F. Xue, H. C. Sun, and G. Q. Zhou, 2015: The El Niño-Southern Oscillation cycle simulated by the climate system model of Chinese Academy of Sciences. *Acta Oceanologica Sinica*, **34**(1), 55–65, https://doi.org/10.1007/s13131-015-0596-9.

Todd, A., and Coauthors, 2020: Ocean-only FAFMIP: Understanding regional patterns of ocean heat content and dynamic sea level change. *Journal of Advances in Modeling Earth Systems*, **12**, e2019MS002027, https://doi.org/10.1029/2019MS002027.

Walsh, J. E., W. L. Chapman, and F. Fetterer, 2015: Updated 2016. Gridded Monthly Sea Ice Extent and Concentration, 1850 Onwards, Version 1.1, National Snow and Ice Data Center (NSIDC).

Winton, M., S. M. Griffies, B. L. Samuels, J. L. Sarmiento, and T. L. Frölicher, 2013: Connecting changing ocean circulation with changing climate. *J. Climate*, **26**, 2268–2278, https://doi.org/10.1175/JCLI-D-12-00296.1.

Xie, P., and G. K. Vallis, 2012: The passive and active nature of ocean heat uptake in idealized climate change experiments. *Climate Dyn.*, **38**, 667–684, https://doi.org/10.1007/s00382-011-1063-8.

Zhang, H., and Coauthors, 2020: Description and climate simulation performance of CAS-ESM version 2. *Journal of Advances in Modeling Earth Systems*, **12**, e2020MS002210, https://doi.org/10.1029/2020MS002210.

Zhang, H., M. H. Zhang, and Q. C. Zeng, 2013: Sensitivity of simulated climate to two atmospheric models: Interpretation of differences between dry models and moist models. *Mon. Wea. Rev.*, **141**, 1558–1576, https://doi.org/10.1175/MWR-D-11-00367.1.